Disruption of orbitofrontal-hypothalamic projections in a murine ALS model and human patients

Authors: David Bayer[1,2], Stefano Antonucci[1], Hans-Peter Müller[1], Luc Dupuis[3], Tobias M. Boeckers[4,5], Albert C. Ludolph[1,5], Jan Kassubek[1], Francesco Roselli[1,5]

E-Mail: david.bayer@uni-ulm.de, stefano.antonucci@uni-ulm.de, hans-peter.mueller@uni-ulm.de, ldupuis@neuro-cnrs.unistra.fr, tobias.boeckers@uni-ulm.de, albert.ludolph@rku.de, jan.kassubek@uni-ulm.de, francesco.roselli@uni-ulm.de

Affiliation:
1. Dept. of Neurology, Ulm University, Ulm DE
2. CEMMA (Cellular and Molecular Mechanisms in Aging) research training group, Ulm DE
3. University of Strasbourg
4. Institute of Anatomy and Cell Biology, Ulm University, Ulm DE
5. German Center for Neurodegenerative Diseases-DZNE, Ulm DE

Corresponding authors: Francesco Roselli,
Center for Biomedical Research (ZBF)
Helmholtzstrasse 8-89081 Ulm (DE)
Phone: 0049-0731-500-63147
Email: francesco.roselli@uni-ulm.de

Abstract

Increased catabolism is a new clinical manifestation of Amyotrophic Lateral Sclerosis. A dysfunction of lateral hypothalamus may drive hypermetabolism in ALS; however, Its causes and anatomical substrates are unknown. We hypothesize that disruption cortico-hypothalamic circuits may impair energy homeostasis in ALS. We used rAAV2 for large-scale projection mapping and image analysis pipeline based on Wholebrain and Ilastik to quantify projections from the forebrain to the latera hypothalamus of the SOD1(G93A) ALS mouse model as well as of the $Fus^{\Delta NLS}$ ALS mouse model. Expanded projections from agranular Insula, ventrolateral orbitofrontal and secondary motor cortex to lateral hypothalamus were found in two independent cohorts of the hypermetabolic SOD1(G93A) ALS model. The non-hypermetabolic $Fus^{\Delta NLS}$ ALS mouse model display a loss of projections from motor cortex but no change in projections from insula and orbitofronal cortex. 3T DTI-MRI data on 83 ALS patients and 65 controls confirmed the disruption of the orbitofrontal-hypothalamic tract in ALS patients. Converging murine and human data demonstrate the selective disruption of hypothalamic inputs in ALS as a factor contributing to the origin of hypermetabolism.

Key words: rAAV2; Agranular Insula; Orbitofrontal Cortex; Lateral Hypothalamus; Hypermetabolism; Amyotrophic lateral sclerosis

Introduction

Amyotrophic lateral sclerosis (ALS) is traditionally conceptualized as a neurodegenerative condition primarily affecting upper motoneurons, located in primary motor cortex, and lower motoneurons, located in spinal cord, whose dysfunction and loss determines a relentless, progressive and ultimately fatal motor impairment [1]. More recently, hypermetabolism has been recognized as an additional, non-motor clinical feature of ALS [2]. Epidemiological surveys have revealed that ALS patients display increased catabolism [2, 3] and pointed out lower body-mass index constitutes a risk factor for ALS [4]. Furthermore, reduced levels of metabolic rate proxies such as plasma lipids and body fat content are predictors of survival of ALS patients [5-7], i.e. weight loss is strongly correlated with shorter survival [8]. Increased catabolism appears to be due to intrinsic hypermetabolism both in ALS patients [9-13] as well as in mutant SOD1 ALS mice [14]. Notably, metabolism and energy balance actually constitute promising targets for intervention, since increasing caloric intake has beneficial effects on survival, particularly on fast-progressing ALS patients [15].

Mechanistic insights into ALS hypermetabolism remain limited. Hypothalamic nuclei receive and integrate inputs coming from a large fraction of the brain [16-19] in order to establish the proper balance of feeding, energy storage and energy expenditure [20]. Thus, disruption of these inputs may be sufficient to drive metabolic imbalances. In fact, the overall architecture between large-scale networks appear to be disturbed in ALS [21-25] and ALS-related pathobiochemistry affects a significant proportion of cortical and subcortical structures, in a pattern evolving with disease progression [26, 27]. We have hypothesized that a similar degree of disruption and remodeling may take place in large-scale networks providing inputs to the

66 feeding-regulating Lateral Hypothalamic Area (LHA) and that such a disruption may coincide
67 with the appearance of the hypermetabolic phenotype. We have now identified the selective
68 disruption of projections from insular and orbitofrontal cortex to LHA in ALS mouse model as
69 well as in human ALS patients by a combination of retrograde rAAV-2 tracing and MRI-DTI tract
70 tracing.
71
72 **Methods**
73
74 *Animals*
75 All experimental procedures involving animals were performed in agreement with the
76 guidelines for the welfare of experimental animals issued by the Federal Government of
77 Germany; all experiments were approved by the Regierungspräsidium Tübingen under the
78 animal license- number 1390 and by the Ulm University Tierforschungszentrum committee. No
79 effort was spared to implement "3R" guidelines for animal experimentation.
80 We obtained from Jackson Laboratories the following strains: B6SJL73 Tg(SOD1*G93A)1Gur/J
81 (high-copy), (henceforth mSOD) and B6.Cg-Gt(ROSA)26Sor$^{tm6/(CAG74ZsGreen)Hze/J}$ (henceforth
82 ZsGreen). To generate the mSOD/ZsGreen double transgenic mice, hemizygous mSOD males
83 were crossed with homozygous ZsGreen$^{+/+}$ females as previously reported [21]; the progeny
84 included mSOD^{+}/ZsGreen$^{+/-}$ mice at the expected mendelian rate. mSOD^{+}/ZsGreen$^{+/-}$ are
85 henceforth going to be labelled mSOD1 and mSOD^{-}/ZsGreen$^{+/-}$will be labelled WT.
86 The heterozygous B6.Fus$^{\Delta NLS/+}$ (henceforth Fus) were provided by Luc Dupuis from the Faculté
87 de Médecine, Strasbourg, France [28]. For the generation of Fus/ZsGreen double transgenic

mice, heterozygous Fus males were crossed with homozygous ZsGreen$^{+/+}$ females. The progeny included Fus^{-}/ZsGreen$^{+/-}$ mice at the expected mendelian rate. Fus^{-}/ZsGreen$^{+/-}$ are henceforth going to be labelled kiFUS.

Mice were housed at 2 - 5 animals per cage, with unlimited access to food and water, a light/dark cycle of 12/12 hr and humidity between 40% and 60%. All mice expressing mSOD were routinely tested for motor impairment and euthanized in case of overt motor disability. Since male and female mice have differ substantially in progression rates of clinical and biological manifestation of motoneuron disease (e.g. [29]), the present study focused on male mice only.

Viral vectors

Retrograde rAAV2 [30] vectors encoding for the pmSyn1-EBFP-Cre (addgene plasmid # 51507; kindly donated by Hongkui Zeng [31]),were obtained from Addgene.

Intracerebral injection

Intracerebral injections of rAAVs were performed as previously reported [21]. Briefly, 1µl of viral suspension with a titer of $3x10^{12}$ vg/ml and 1 µl of 1% of Fast Green were freshly mixed and 300 nl of the mixture was loaded into a pulled-glass capillary. Pulling parameters were optimized to obtain a long and tapering capillary tip. Mice were pre-treated with buprenorphine (0.1 mg/kg) and meloxicam (1 mg/kg) 20 min before being anesthetized with 5% sevoflurane /95% O_2 ; mice were then positioned into a stereotactic frame (David Kopf) and kept under continuous

anesthesia with 3% sevoflurane/97% O_2. Mice were positioned on a heated pad connected to a closed-loop system to maintain body temperature, monitored by a rectal probe, at 37°C. Upon incision of the scalp, a burr hole was prepared using a hand-held microdrive aiming the LHA at AP = -1.20, ML = -1.25, DV = -4.70 (according to Paxinos atlas, 2nd edition [32]) refined for the mouse strain under consideration of the age).

Under visual control, the pulled-glass capillary (tip closed) was moved into the drilled hole and gently pushed down to verify that meninges could be penetrated without deflection of the capillary. Thereafter, the pulled-glass capillary was withdrawn and opened at the very tip by gently touching with a microscissor. Before lowering the pulled-glass capillary to the final position inside the brain, a thin layer of $DPBS^{+Ca/+Mg}$ was applied, generating a virus-free tip by capillary force. Since brain tissue might absorb some of the liquid out of the pulled-glass capillary by its own tissue/capillary force, during further movement, the pulled-glass capillary was lowered not slower than 2 mm/s. The viral suspension was injected using a Picosprizer microfluidic device; injection was performed during 5 min. The duration of one pulse was 10 ms; since the opening diameter of each capillary could be slightly different, the injection pressure was adapted (between 20 and 60 psi) to ensure a constant overall flow rate of 50-60 nl/min. After injection, the capillary was kept in place for 15 min and then removed with a continuous movement (1 mm/s). Remaining pressure in the capillary was released before withdrawing it to prevent any residual virus suspension to be discharged into the capillary thread.

Immunohistochemistry

Mice (mSOD) were sacrificed at P (post-natal day) 40 (injection at P25) or at P110 (injection at P95); Fus mice were injected at P255 and sacrificed at P270.

Mice were trans-cardially perfused with PBS and then 4% PFA in PBS; after 18h of post-fixation in 4% PFA, brains were cryoprotected in 30% Sucrose/PBS, embedded in OCT and serially sectioned using a *Leica CM1950 cryostat* into 70 µm sections from AP +2.6 mm to -3.0 mm as previously reported [21].

The ZsGreen reporter did not require immunodetection since the native signal was very strong. For dedicated experiments, immunostaining for SOD1 (Anti SOD1, Sigma-Aldrich, HPA001401, 1:500), misfolded SOD1 (Misfolded SOD1 (B8H10), MédiMabs, MM-0070-p, 1:250) and Fus (Anti Fus, Sigma-Aldrich, HPA008784, 1:300) was performed.

Briefly, sections were blocked in blocking solution (3% BSA, 0.3% Triton in PBS) for 2h at room temperature (rt). Primary antibody was diluted in blocking solution and incubated at 4°C for 72h. Secondary antibody (Invitrogen, Donkey anti-rabbit Alexa Fluor 568, # A10042; Donkey anti-mouse Alexa Fluor 647, # A31571; anti-guinea pig 405) was applied diluted 1:500 in blocking solution after three washing steps (PBS 20 min at rt) and incubated for 2h at rt. Subsequently sections were washed three times again and mounted using Gold Antifade Mountant (Invitrogen #P36930).

Image acquisition

Glass slides of serially-sectioned brains were first subject to visual assessment using a Leica DMIL equipped with a 2.5x/0.07 objective; brains that were injected in the wrong location or displayed obvious macroscopic artifacts were excluded at this stage and not processed further.

153 The remaining set of brain sections were imaged in full using a slide-scanning microscope (Leica
154 DMI6000B) equipped with a 5x/0.12 objective and exposure time ranging between 300 ms (405
155 nm) to 800ms (647 nm). All images were saved at 15304 x 28295 resolution with 16-bit depth.
156 Images of the cortical areas immunostained for misfolded SOD1 were acquired using a Zeiss
157 LSM710 confocal laser scanning microscope equipped with a 20x air objective. In total, 15
158 optical sections each 1µm-thick were acquired for each region of interest.
159
160 *Neuron mapping*
161 A multiple software approach was devised to analyze brain section images and properly
162 parcellate and quantify projections from cortex to LHA; the pipeline is summarized in Fig. 1A
163 and is reported here in detail.
164 Anatomical annotation **–** Firstly, a custom *Fiji* [33] macro allowed extracting single brain sections
165 from whole microscopic slide images while appending serial numbers. Hands-on registration of
166 coronal brain sections was performed by means of *WholeBrain* package in *R* [34], laying its
167 foundations on the Allen Brain mouse reference Atlas (ABA version 2011 [35]). In view of
168 accounting for tilted sections (as compared to the original ABA coronal planes) and for biological
169 inter-individual brain differences, a series of easily recognizable anatomical landmarks were
170 chosen to appropriately map the regions of interest (ROIs) along the anterior-posterior (AP)
171 axis, as shown in the Supplementary Table 1. The stereotactic coordinates were determined
172 with *openbrainmap.org*.
173 Neuron segmentation **–** Despite the flexibility of the parameters of the built-in segmentation
174 functions in *WholeBrain*, a systematic underestimation of neuronal counts was noticeable in

areas with high neuronal density, such as the frontal cortex, whereas a systematic overestimation of neuronal counts took place in areas with low neuronal density, due to the inclusion of segments of dendrites as purported neurons. In order to avoid the warping of the neuronal counts because of these opposing biases, a separate strategy was pursued for neuron segmentation in single brain ROIs alone. RGB images with single region outlines were generated as explained in https://gitter.im/tractatus/Lobby and imported in *Fiji* [33]. Another *Fiji* macro was then designed to mask and resize the RGB image in order to have a perfect match of the original high-resolution image, to convert the former to HSB Stack, recover the outline of the brain ROI and use it to crop the latter.

Ilastik toolkit [36] subsequently served a double purpose. The Pixel Classification workflow enabled to discriminate neurons (foreground) from neuron-devoid brain architecture (background); the resulting binary images (Fig. 1A, 4.3) were fed to a final *Fiji* macro to crop highly-resolved brain ROIs (Fig.1A, 4.2) to smaller ROIs containing neurons only (Fig.1A, 4.6) and exclude brain ROIs without LHA-projecting *somata* from further analysis. This step proved crucial to resort to a highly trained Cell Density Counting *Ilastik* suite, since brain architecture removal reduced the chance of generating false positives and drastically lessened the burden on the RAM.

Ilastik training

For both pixel classification and cell density counting workflows, σ values of 1.0, 1.6, 3.5 and 5.0 were selected for the following features: Gaussian Smoothing, Laplacian of Gaussian, Gaussian Gradient Magnitude, Difference of Gaussian, Structure Tensor Eigenvalues, Hessian of Gaussian

Eigenvalues. Twenty randomly selected whole-section images were sufficient for Pixel Classification training; batch processing generated simple-segmentation.tiff (Figure1, A, 4.3) images.

On the other hand, the Cell Density Counting classifier required a total of 250 randomly selected images for training. As displayed in figure 1B, after annotating 100 images the training effect had already reached saturation. Since accuracy of less than 90% seemed not satisfying enough, additional 150 images were annotated to tweak out a few more percentages in accuracy. Furthermore, we adapted the parameters of the implemented *Random Regression Forest* algorithm (described in more detail in [37]), namely number and maximum depth of the trees (Ntrees = 20, MaxDepth = 80), achieving a final accuracy of 94% by comparing counts to a selection of 100 randomly selected and manually counted images. Random sampling of probability maps exported upon batch image processing provided a further quality control (Fig.1A, 5.2).

Determination of single brain region and injection site volumes

Volume measurements were performed with yet another custom macro in *Fiji*, measuring the area of individual scaled cropped.tiff images (Figure1, A, 4.2) and multiplying by the thickness of a single section (70 µm). Injection site volumes were determined by manually defining their cross-section in every brain slice at a set image contrast and once again multiplying such areas for the section thickness. Brains with injection sites bigger than 1 mm^3, mislocalized position or displaying a virus backflow (visible in dorsal regions with respect to the LHA) bigger than 10% of the whole injection site itself were excluded from further analysis.

Determination of misfSOD1 burden

A dedicated macro in Fiji was used to create a selection of misfSOD positive cells by applying the RenyiEntropy [38] thresholding and subsequent background subtraction (rolling ball radius = 20 px) and gaussian blurring (σ = 1). Afterwards, the area was measured by restoring the selection in the original image

MRI scanning of DTI data in ALS patients

DTI scanning study included 83 ALS patients (58 ± 14 years, 49m, ALS-FRS-R 40 ± 6, disease duration 19 ± 16 months) and 64 controls (52 ± 11 years, 33m) according to a standardized protocol (for details see [39]). DTI data were acquired on a 3.0 T head scanner (Allegra, Siemens Medical, Erlangen, Germany). The standardized DTI scanning protocol was as follows: 49 gradient directions (b = 1000 s/mm²) including one b = 0 gradient directions, 52 slices, 96 x 128 voxels in-plane, slice thickness 2.2 mm, in-plane voxel size 2.2 mm x 2.2 mm, echo time 85 ms, repetition time 7600 ms. All participating patients and controls provided written informed consent for the study according to institutional guidelines. The study was approved by the Ethical Committee of the University of Ulm (reference #19/12).

DTI analysis

The DTI analysis software Tensor Imaging and Fiber Tracking (TIFT [40]) was used for post processing and statistical analysis as previously described [39]. In brief, stereotaxic normalization to the Montreal Neurological Institute (MNI) space was performed iteratively

using study-specific templates. To map white matter microstructure, fractional anisotropy (FA) maps were calculated from the stereotaxically normalized DTI data sets of all subjects. A Gaussian filter of 8 mm full width at half maximum was applied for smoothing of FA maps for a good balance between sensitivity and specificity [41] and FA maps were corrected for the covariate age. Tractwise fractional anisotropy statistics (TFAS) was performed by statistically comparing the FA values between the two subject groups in a given tract system [42]. The following tract systems were focussed on: a tract from orbitofrontal regions to the hypothalamus (orbitofrontal-hypothalamic tract), a tract from the hypothalamus to the insula (insular-hypothalamic tract), the cingulate-hypothalamic tract, and the corticospinal tract as a reference. Consequently, a tract-of-interest (TOI) analysis allowed for quantification of microstructural alterations in these tract systems.

Statistical analysis

The statistical analysis was performed with the *GraphPad8* software suite. Comparison of the neuronal counts (absolute counts or normalized) was performed by two-way ANOVA (genotype x structure design) using Sidak´s post-hoc multiple comparisons correction; corrected p values are provided. Normalization was obtained dividing the absolute number of neurons in each structure for the total number of neurons counted in that brain and multiplying the ratio for 50,000. Comparison of total neuronal counts was performed by two-tailed unpaired Student´s t-test. Comparison of misfSOD1 burden was performed by one-way ANOVA with Tuckey´s post-hoc test.

Results

Enhanced semi-automated mouse brain segmentation with neuronal annotation for global quantification of projections with single-cell resolution.

In order to build a quantitative and anatomically accurate map of projections from cortical and subcortical areas to the lateral hypothalamus, first we set out to establish a reliable approach to identify neurons and register their position within the structure classification of the Allen Brain Anatomical reference Atlas (Fig. 1A). The image batch for software training was obtained by injecting the retrograde rAAV2 (rAAV2-retro) into the LHA of two ZsGreen reporter mice. The latter were sacrificed 15 days later and the fixed brain was serially sectioned in 70 µm-thick sections; the whole glass slide with mounted sections was scanned using a Leica epifluorescence microscope. Each atlas plate was warped onto the brain section by defining an appropriate number of corresponding anatomical landmarks with *WholeBrain* (see the Methods section), thereby matching the atlas coordinates with the actual brain sections and allowing a proper anatomical annotation (Fig. 1A, 2). Single structure outlines (cortical layers, subcortical structures, e.g. fig. 1A, 4.1) were extracted using a dedicated *R* script, size-corrected and re-overlapped onto the original image in *Fiji*; the corresponding area of the original image was then cropped (Fig. 1A, 4.2), resulting in the unpacking of the original single-section into several hundreds cropped pictures (each image was coded to be later identified), resulting in >100,000 pictures per brain. In order to identify and count the number of neurons in each fragment, *Ilastik* software suite was employed. Simple foreground/background segmentations were generated by resorting to the pixel classification workflow. This allowed to automatically clear

most of the brain autofluorescence background in *Fiji* (Fig. 1A, 4.6). This step enabled the improvement of the discrimination of few ZsGreen+ neurons in ROI containing many more dendrite stretches and artifacts, and also reduced the computational burden placed on *Ilastik* cell density classifier and therefore minimizing the chance of generating artifactual counts. *Ilastik cell density* classifier was trained with 250 randomly selected ROI images that were annotated by a human operator; the accuracy of software reached 86% after 100 images and achieved a final 94% peak (Fig. 1B) by improving the performance of the *Random Regression Forest* algorithm with 150 additional images and tuning its parameters (trees number and depth; see Methods). The whole procedure was then sequentially implemented so that neuronal counts for each picture from every section were annotated and logged together with the anatomical location within the hemisphere and the brain section as well as with the rostro-caudal serial number of the section itself.

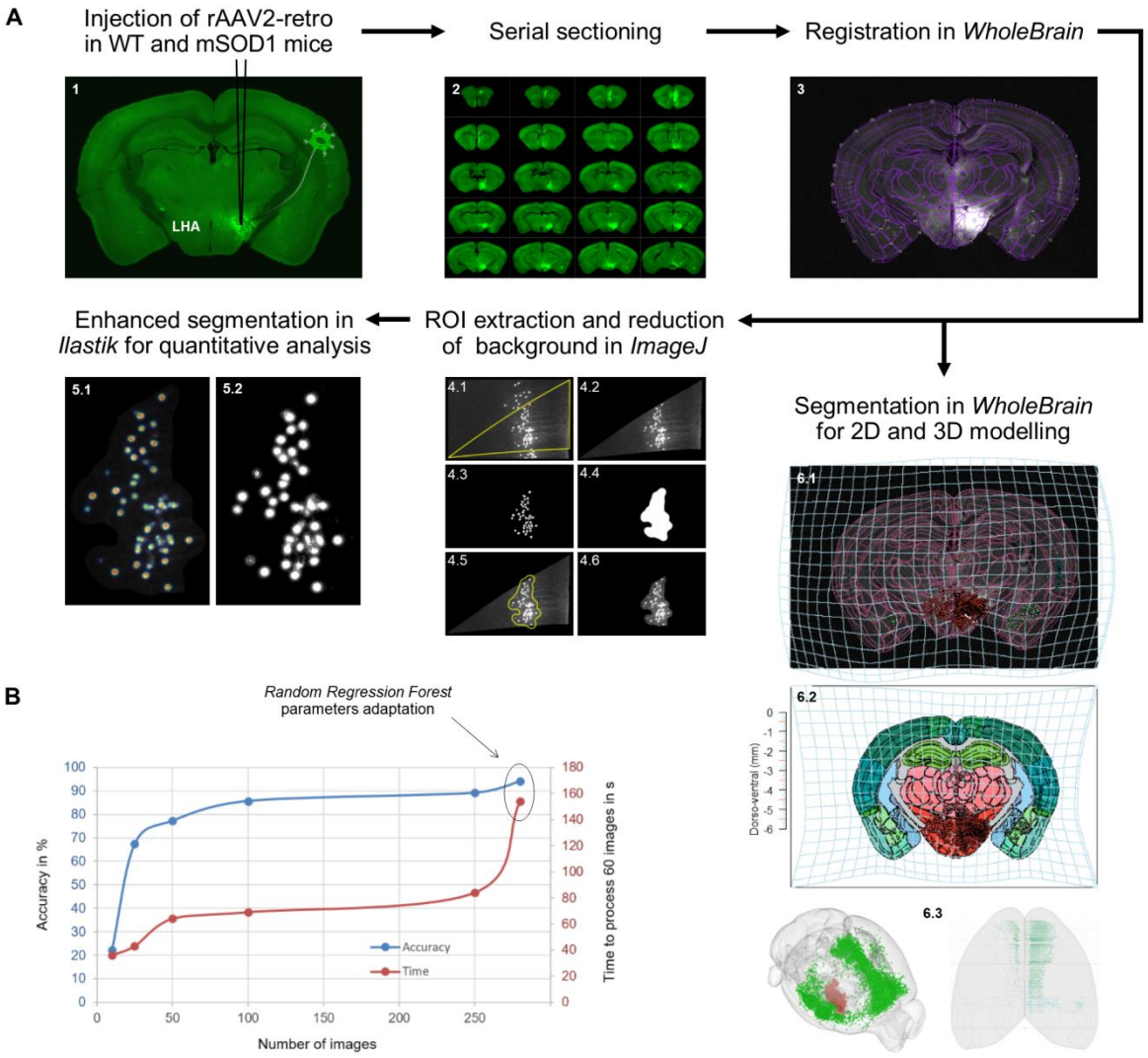

303

304 ***Figure 1***: Pipeline for the quantitation of forebrain projections to LHA. A: Neurons projecting to
305 LHA are identified by injecting rAAV-retro encoding Cre in the LHA of WT (or mSOD1) carrying a
306 floxed ZsGreen reporter allele (panel 1). Brains are serially sectioned (2) and each section is
307 manually registered in *WholeBrain* (3). To obtain a precise quantification of the neurons in each
308 anatomical structure, registered sections are parcellated and background-corrected in *ImageJ*
309 (panel 4) and the parcellated images are segmented using a purpose-trained *Ilastik* (density
310 counting workflow) (5) to obtain the final neuronal counts per image. The *WholeBrain* dataset is
311 also used to derive an independent anatomical annotation in the Allen Brain Atlas (backward
312 warp transform field (atlas plate to section) 6.1, forward warp transformation field (section to
313 atlas plate) 6.2) and 3D reconstructions (6.3). B: Training of *Ilastik* cell density counting.
314 Accuracy improvement of the classifier according to the amount of images used for training. The
315 increasing need of computing power is indicated by the time needed to process 60 Images.
316 Accuracy was calculated by comparing randomly selected and manually counted images. Using a
317 total of 250 images and adapting the parameters for the *Random Regression Forest*, a final
318 accuracy of 94% was achieved.

Disrupted cortico-hypothalamic projections in symptomatic mSOD1 ALS mice

We exploited our enhanced registration-segmentation-annotation pipeline to establish whether the large-scale architecture of the projections to LHA was altered in the mSOD1 mice at a symptomatic stage (i.e., when body weight loss has appeared and clinical score is 2). To this aim, 20 mSOD1/ZsGreen+ and 20 WT/ZsGreen+ mice were injected at the age of P95 with rAAV2-retro [30] encoding for Cre under the human synapsin promoter in the Lateral hypothalamic area (LHA; Fig. 2A). All neurons projecting to the site of injection would take up the rAAV2-retro, express the Cre recombinase and appear ZsGreen+. Mice were sacrificed 15 days later. Upon serial sectioning, a series of quality control criteria were applied and brains displaying i) improper location of the injection site ii) injection volume larger than the boundaries of the LHA iii) large number of neurons infected along the thread of the injection capillary iv) low (<25,000) overall number of ZsGreen+ neurons were excluded from further analysis. Six brains for each genotype were then considered for further quantification. These brains were randomly divided in two cohorts: cohort 1 was subjected to *WholeBrain* parcellation and cohort 2 was left for confirmation (see below). Once cohort 1 brains were processed through the *WholeBrain*-registration and annotation pipeline, we identified an average of about 50,000 neurons projecting to the LHA in WT mice; when the brainstem was excluded (because anatomical annotation of brainstem nuclei was judged unreliable based on visual inspection of the *WholeBrain*-overlapped images), we identified 84 cerebral areas projecting to the LHA (full list with absolute and normalized neuronal counts is provided in the Supplementary Table 2). Projections were identified from a large fraction of the forebrain, with the largest component provided by limbic areas such as Anterior Cingulate Area (ACA), Prelimbic Cortex (PL),

341 InfraLimbic Area (ILA), Agranular Insula (AI), as well as from subcortical structures belonging to
342 the limbic system such as Basolateral and Basomedial Amygdala (BLA and BMA, respectively).
343 Intriguingly, substantial projections were identified from motor areas (primary and secondary),
344 from primary sensory areas (gustatory, auditory, olfactory/piriform, visual cortex) and from
345 basal ganglia (Dorsal Putamen, DP), underscoring the breath of integration taking place in LHA.
346 The same structures appeared to project to LHA from ipsilateral and contralateral hemispheres,
347 although the contralateral contribution appeared to be substantially smaller (approx. 40,000
348 neurons from the ipsilateral hemisphere vs 10,000 from the contralateral in WT animals).
349 In order to obtain a pertinent comparison (i.e., excluding areas with counts <100 neurons) of
350 projections in WT and mSOD1 mice, we contrasted the absolute neuronal counts in 28 areas
351 (accounting for approx. 50% of the total projections, maintaining ipsi and contralateral dataset
352 distinct; PL and orbitomedial cortex as well as lateral/ventrolateral orbitofrontal cortex -ORBl/vl-
353 and AI were grouped together due to the uncertainty in establishing their borders and in
354 agreement with functional similarity. While the overall pattern of projections to LHA in
355 symptomatic mSOD1 mice was comparable to the WT ones, the cumulative absolute counts of
356 ZsGreen+ neurons for the 28 structures were significantly increasedin the mSOD cohort
357 considering the absolute counts (p=0.02; Supplementary Fig. 1-A). We contrasted the absolute
358 counts for each of the 28 areas in WT and mSOD1 mice (Supplementary Fig. 1- 1B). Two-way
359 ANOVA revealed a significant effect of genotype ($F_{1,112}$=105.70, p<0.0001) and post-hoc analysis
360 (Sidak´s multiple comparisons test) revealed significant expansion of the projections from ACA
361 (p<0.0001), ILA (p=0.009), ORBl/vl+AI (p<0.0001), Tenia Tecta (TT; p=0.0365), secondary motor
362 cortex (MOs, p<0.0001) and piriform cortex (PIR; p=0.0005). In order to compensate for the

363 variable total number of infected neurons in each individual brain, we then normalized the
364 absolute counts of neurons projecting to LHA to a nominal of 50,000 neurons, so to compute
365 the relative contribution of each area to the total input to LHA. Upon normalization, the 28
366 areas in object amounted for a comparable total number of neurons (Fig. 2B). Two-way ANOVA
367 on normalized data revealed once again a significant effect of genotype ($F_{1,112}$= 7.31, p=0.0079)
368 and post-hoc analysis revealed a significant increase in projections from ORBl/vl+AI (p=0.0012)
369 and from MOs (p=0.0006; Fig. 2C; also visualized in the 2D projections, Supplementary Fig. 1-C-
370 D as well as in the 3D Wholebrain reconstruction, Fig. 2D). The remaining 26 structures
371 displayed only non-significant trends toward expanded projections (PIR: p=0.21; ILA: p=0.32) or
372 no difference in the size of the neuronal population projection to LHA (Fig. 2C). When the
373 projections from the contralateral hemisphere were contrasted, we detected an effect of
374 genotype in the absolute counts (two-way ANOVA $F_{1,112}$= 31.49 ; p<0.0001) that was traced in
375 post-hoc test (Sydak´s) to a significant expansion of projections from ACA (p=0.0008), ILA and
376 PL+ORBm (both p<0.0001) (Supplementary Fig. 2- 2A-B). However, when the absolute counts
377 were normalized to account for the total number of ZsGreen^{+} neurons in each brain, no
378 significant differences were identified between the genotypes (two-way ANOVA, $F_{1,112}$= 0.31,
379 p=0.57; Supplementary Fig. 2-C).
380
381 Since mice with neurodegenerative phenotypes may display cortical atrophy [43], we used the
382 *WholeBrain* registration to measure the volume of each cortical structure and compensate for
383 eventual volume loss. Indeed, we identified a significant loss of volume in mSOD1 mice (two-
384 way ANOVA $F_{1,112}$=28.80, p<0.0001) which was traced by post-hoc test (Sidak´s.) to the atrophy

385 of MOp (p=0.008) and SS (p<0.0001) with only a trend seen for MOs (p=0.33) (Supplementary
386 Fig. 3). Notably, ORBl/vl+AI and MOs did not display significant changes in volume.
387 Thus, in symptomatic mSOD1 mice (displaying the hypermetabolic phenotype), a substantial
388 remodeling of cortico-hypothalamic projections takes place, in particular from ORBl/vl+AI and
389 MOs.
390

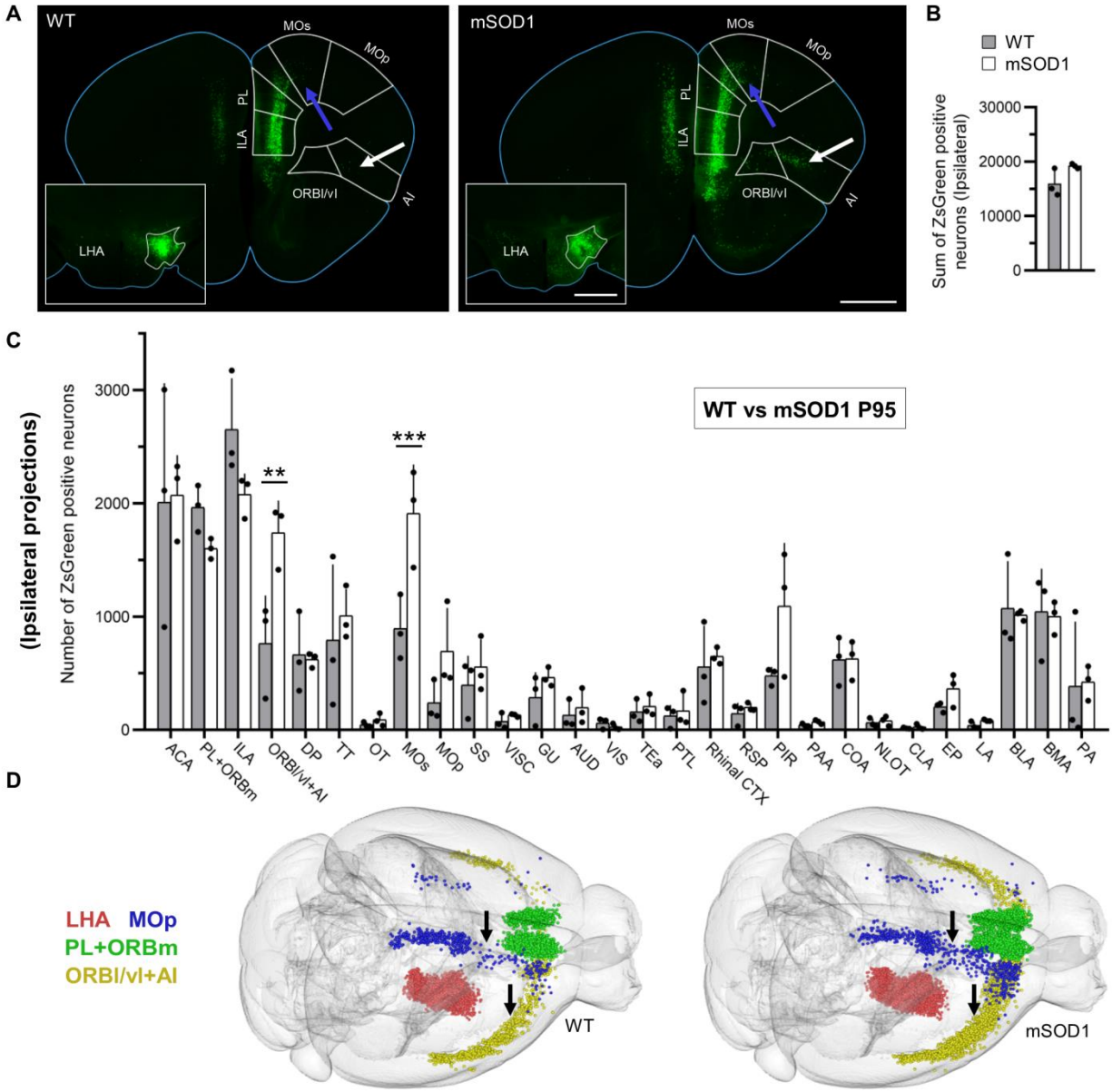

391

Figure 2: Altered cortico-hypothalamic projection pattern in mSOD1 mice at P95. A: Representative frontal brain sections of WT and mSOD1 mice depicting projections from ORBl/vl+AI (significantly increased, arrow), PL+ORBm, ILA, ACA, MOs and MOp to LHA. Inset: representative injection sites in LHA for WT and mSOD1 mice. White outlines represent LHA boundaries. B: Sum of neurons projecting from selected 28 areas. No difference is detected in the summarized number of neurons projecting to LHA in WT and mSOD1 from the ipsilateral hemisphere (n=3). C: Quantification of the number of neurons (normalized for total neuronal counts) projecting to LHA from 28 brain structures in WT and mSOD1. A significant increase in projections from ORBl/vl+AI (p=0.0012) and from MOs (p=0.0006) is detected. D: Representative *WholeBrain* volume reconstructions of neurons projecting to LHA in WT and mSOD1 mice. Expansion of projections from MOs (blue) and ORBl/vl+AI (yellow) are visible (arrows). Bars show mean ± SD. Scalebars 1 mm . *$p < 0.05$, ***$p < 0.001$, ****$p< 0.0001$.

Validation of cortico-hypothalamic projections abnormalities in independent operator-registered brain cohorts

Since the identification of different cortical and subcortical areas was based on the assumption of the overall similarity of the brain of mSOD1 and WT mice, we took into consideration the possibility that biases in the identification of anatomical areas could have been introduced by *WholeBrain* (e.g., because of atrophy), thereby mis-attributing neurons to cortical areas. Therefore, we set out to validate our findings using the brain cohort 2 (n=3 for WT and mSOD1; LHA injection; Supplementary Fig. 4-A). These brain images were subjected to manual registration, i.e. each anatomical structure and cortical area was identified by a genotype-blind operator using structural landmarks (Supplementary Table 1) and individually cropped out of each image of each section of the brain. This approach was substantially slower than the registration by *WholeBrain* (it required >500h of operator´s work time for the whole dataset to be registered and cropped). The individual pictures cropped out of the brain images were then subject to neuronal counts by *Ilastik* (since the accuracy and reproducibility of this step was already established and quantified). In the manually-annotated dataset, the total number of

neurons projecting to LHA was found to be not significantly different in the mSOD1 compared to the WT (Supplementary Fig. 4-B). First, we considered the absolute neuronal countings: the contrast of the two genotypes (ipsilateral hemisphere) revealed a statistically significant difference (two-way ANOVA $F_{1,112}$=6.28 ; p=0.0136) which was further explored in post-hoc comparison (Sydak´s) revealing a significant expansion of projections from ORBl/vl+AI in mSOD1 mice (p=0.035) (Supplementary Fig. 4-C). Upon normalization we once again detected a significant effect of genotype (two-way ANOVA $F_{1,112}$=23.78 ; p<0.0001) with post-hoc revealing significant differences in ORBl/vl+AI (p<0.0001), ILA (p=0.001) and PIR (p<0.0001) (Supplementary Fig. 4-D). When the projections from the contralateral hemisphere were considered, no overall, genotype specific or area correlated effect was found in the absolute counts (Supplementary Fig. 5-B); however, upon normalization, a statistically significant loss of projections from PL+ORBm was identified (p<0.0001), together with a strong trend toward increased projections from ORBl/vl+AI (p=0.072) (Supplementary Fig. 5-C). Thus, the manually-registered dataset displayed substantial similarities with the *WholeBrain*-registered dataset (expansion of the projections from ORBl/vl+AI) but also a major discrepancy: increased projection from ILA to LHA in the manual dataset and no difference in MOs projections, whereas the opposite was detected by *WholeBrain*. Upon closer inspection of MOs projection to LHA we realized that the boundaries of MOs and ILA display a high degree of subjectivity when manually drawn and it is highly likely that MOs neurons were allocated to adjacent areas in the same way ILA was moved to neighboring areas in the dataset parcellated by the human operator.

Nevertheless, the manually-registered independent dataset confirmed the expansion of projections from AI/ORBvl to LHA.

Unaltered projections to LHA in early presymptomatic mSOD mice

Remodelling of large-scale cortical circuits has been previously reported [21] and appears to progress over time; nevertheless, early signs of increased projections from somatosensory cortex (SS) to primary motor cortex (MOp) were detected already at early presymptomatic stages. We set out to verify if the increased projections from AI/ORBvl appeared only late, in coincidence with the appearance of the metabolic phenotype, or if they were present already at presymptomatic stage (and possibly of developmental origin). To this aim, we injected rAAV2-retro in the LHA of WT or mSOD1 at the age of P25 (Supplementary Fig. 6-A) and sacrificed the mice at P40. After quality control, we assessed the forebrain projections to LHA in the two genotypes (n=3 for each). The overall pattern of projections to LHA at P25 was comparable to the one observed at P95 and there was no difference in the absolute number of neurons projecting to LHA in the two genotypes (Supplementary Fig. 6-B). The direct contrast of the two genotypes for the absolute and relative contribution of 28 selected ipsilateral structures revealed a genotype effect in absolute (two-way ANOVA: $F_{1,112}$= 12.55 ; p=0.006) but not in the normalized dataset (two-way ANOVA: $F_{1,112}$= 1.83 ; p=0.1779). However, in both cases the post-hoc comparison did not reveal any significant difference between the two genotypes in any of the considered structures (Supplementary Fig. 6-C,D). Likewise, no statistical difference was found in the sum of projection from the contralateral hemisphere in absolute counts (Supplementary Fig. 7-A), but significant increase in projections from ACA was identified (p=0.0078) (Supplementary Fig. 7-B). Nevertheless, this difference disappeared after normalization (Supplementary Fig. 7-C) and no differences are perceptible in the 3D brain

reconstructions (Supplementary Fig. 7-D). These findings suggest that altered AI/ORBvl connectivity to LHA arises during disease progression and it is not a developmental feature of mSOD1 brain architecture.

ALS-related pathology in the AI/ORBvl of mSOD1 mice

We further investigated the degree of involvement of cortico-hypothalamic projections in ALS by assessing the burden of misfolded SOD1 pathology in cortical areas projecting to LHA, in particular those displaying altered connectivity compared to WT animals. We injected WT or mSOD1 mice with rAAV2-retro in LHA at P95 and sacrificed them at P110. Brain sections encompassing MOp, AI/ORBvl, PL+ORBm, (SS) were immunostained with an antibody recognizing the misfolded conformation of SOD1 (B8H10 [44]) (Fig. 3A-B). The total burden of misfSOD1 was different across the cortical areas (one-way ANOVA $F_{3,20}$=51.26, p<0.0001; MOp vs. ORBl/vl+AI p<0.0001, MOp vs. PL+ORBm p<0.0001, SS vs. ORBl/vl+AI p=0.0014, ORBl/AI vs. PL+ORBm p=0.0006), with MOp displaying the highest burden compared to SS but with ORBl/vl+AI displaying a significantly higher burden than areas showing no increase in projections such as SS or PL+ORBm (Fig. 3A-B). Interestingly, neurons projecting from MOs to LHA display high levels of misfSOD1 accumulation, whereas this is not true for neurons projecting from PL+ORBm and ORBl/vl+AI (Fig.3A).

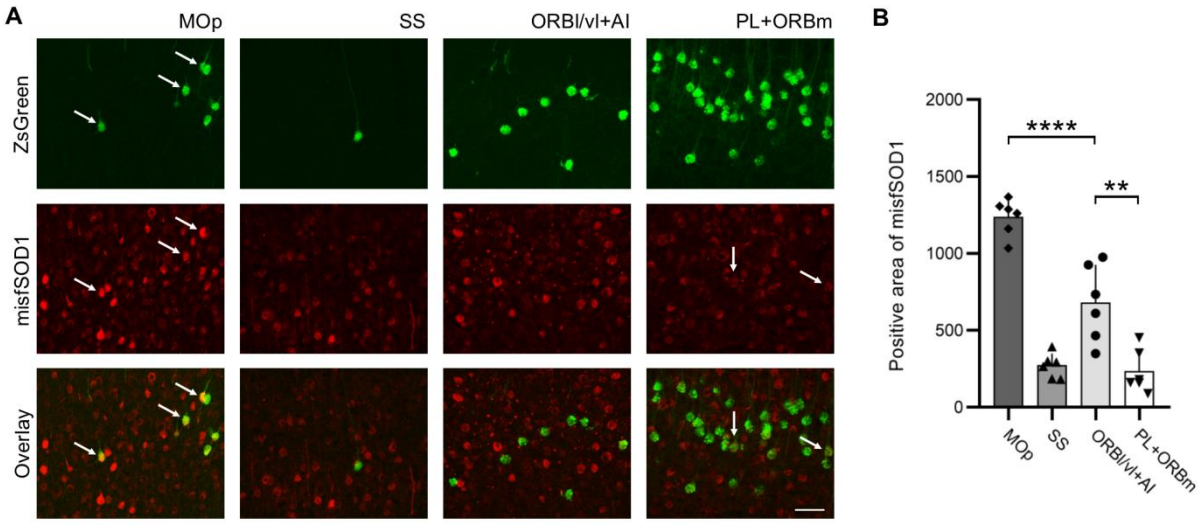

Figure 3: Significant misfolded SOD1 burden in ORBl/vl+AI in mSOD1 mice. A: Representative images of misfSOD1+ cells in MOp, SS, ORBl/vl+AI and PL+ORBm; ZsGreen^{+} neurons projecting to LHA show a strong misfSOD1 burden in MOp (arrows). Other structures show no double positive neurons (SS,ORBl/vl+AI) or weak mSOD burden (PL+ORBm; arrows). B: Burden of misfolded SOD1 (detected by the B8H10 antibody) in MOp, SS, ORBl/vl+AI and PL+ORBm. ORBl/vl+AI displays a burden significantly higher than SS or PL (p=0.0014 and p=0.0006 respectively; areas with unchanged connectivity to LHA) but significantly lower than MOp (p<0.0001). Bars show mean ± SD. Scalebars 50 µm. $^{**}p < 0.01$, $^{****}p< 0.0001$.

Distinct pattern of altered cortical projections to LHA in Fus mice

We further explored the alteration of projections to LHA in ALS in an independent ALS model, the kiFUS mouse. Of note, the kiFUS mouse differs from the mSOD1 mouse because it does not display an overt body-weight phenotype [45] and shows a more limited loss of spinal motoneurons and slower progression [29]. We proceeded with a similar experimental design as for the mSOD1 mice; however, since kiFUS mice display spinal motoneuron loss not before 9-10 months of age, we considered the P255 as “early symptomatic” stage. Therefore, kiFUS mice and their own WT littermates were injected at P255 into the LHA (Fig. 4A and sacrificed at P270 (n=4 for each group). Once again, there was no difference in the overall number of neurons projecting to LHA across the forebrain in absolute counts (Supplementary Fig. 8-A). When the

absolute neuronal counts of each of the 28 areas were contrasted, we detected a significant effect of the genotype (two-way ANOVA $F_{1,166}$=8.583 ; p=0.0039) and post-hoc comparison revealed a significant decrease in kiFUS in projections from ACA (p=0.0385), MOs (p<0.0001) and strong trends for MOp (p=0.1543) and SS (p=0.0848) (Supplementary Fig. 8-B). Upon normalization for 50,000 neurons, a significant difference in MOs was still detected (p<0.0001) together with strong trends for ACA (p=0.1639) and MOp (p=0.136) (Fig. 4B-C and 2D models in Supplementary Fig. 8-C,D). Interestingly, a significant genotype effect was also found in the contralateral hemisphere both in absolute (Supplementary Fig. 9-A,B) and normalized data (Supplementary Fig. 9-C) (two-way ANOVA, $F_{1,166}$= 6.57 ; p=0.0112 and $F_{1,166}$= 4.48 p=0.0356, respectively) and differences were revealed by post-hoc analysis in loss of projections from ACA (p=0.0121 and p=0.0137 in absolute counts and normalized, respectively) and ILA (p=0.0474) in the absolute counts only. Of note, projections from AI/ORBvl were not affected (neither from ipsilateral nor from contralateral). The significant loss of MOs neurons projecting to LHA was especially affecting the most rostral part of MOs, as demonstrated by the 3D reconstruction model of the mouse brain (Fig. 4D). Thus, distinct ALS models with divergent metabolic phenotype display different patterns of altered projections to LHA.

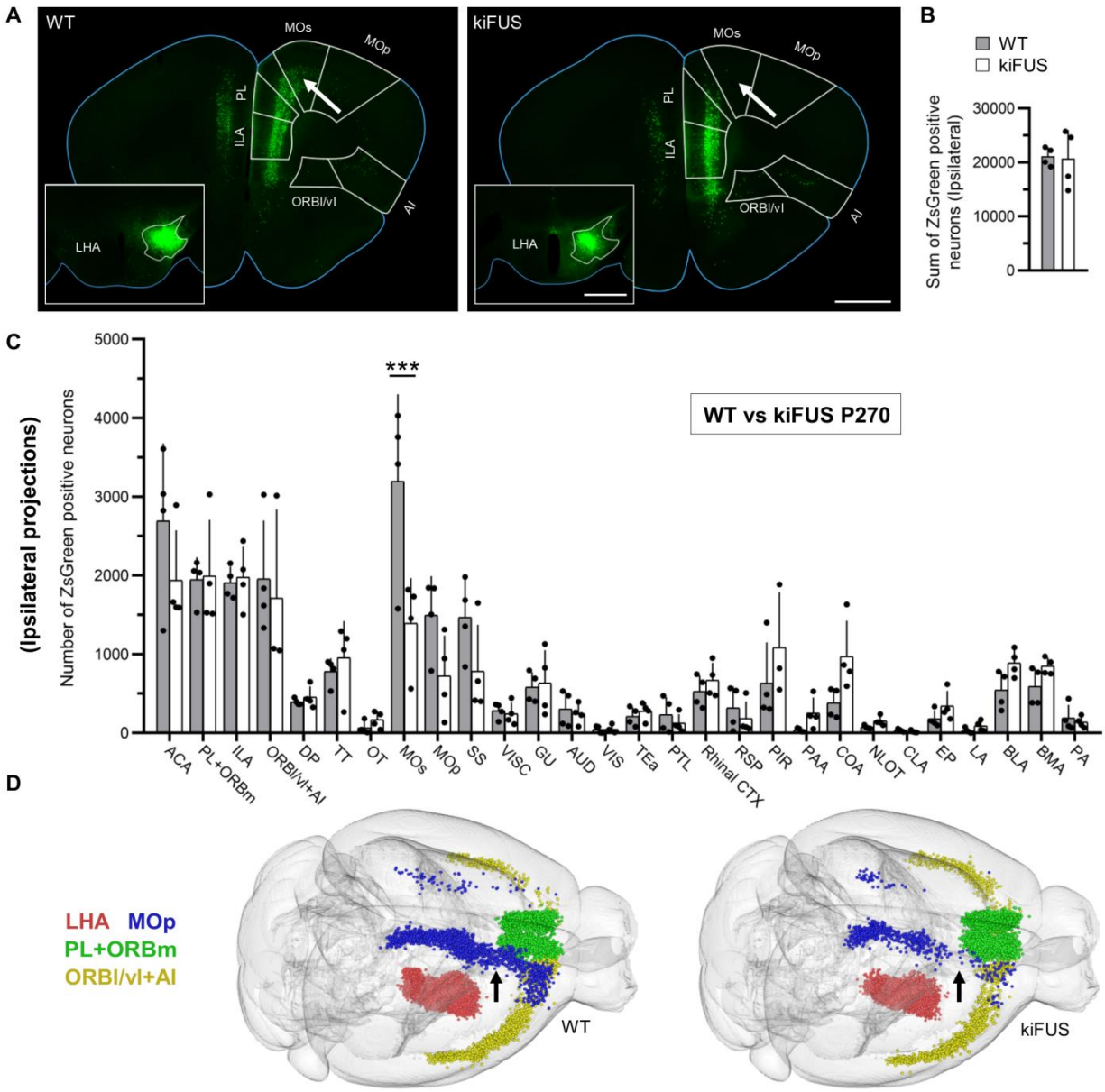

Figure 4: Altered cortico-hypothalamic projection pattern in kiFUS mice at P270. A: Representative frontal brain sections of WT and kiFUS mice depicting projections from MOs (significantly decreased, arrow), PL+ORBm, ILA, ACA, and MOp to LHA. Inset: representative injection sites in LHA for WT and kiFUS mice. White outlines represent LHA boundaries. B: Sum of neurons projecting from selected 28 areas. No difference is detected in the summarized number of neurons projecting to LHA in WT and kiFUS from the ipsilateral hemisphere (n=4). C: Quantification of the number of neurons (normalized for total neuronal counts) projecting to LHA from 28 brain structures in WT and kiFUS. A significant decrease in projections from MOs ($p<0.0001$) and trend toward decrease projection from ACA ($p=0.1639$) and MOp ($p=0.136$) is detected (n=4). D: Representative *WholeBrain* volume reconstructions of neurons projecting to

LHA in WT and kiFUS mice. Loss of projections from the anterior part of MOs (blue) is visible. Bars show mean ± SD. Scalebars 1 mm. *$p < 0.05$, **$p < 0.01$, ****$p < 0.001$.

DTI-MRI reveals altered orbitofrontal-hypothalamic tract in ALS patients.

Finally, we set out to investigate if the selective disturbance in cortico-hypothalamic projections from AI, ORBvl and PL observed in the mSOD1 mice could also be observed in human ALS patients. To this aim, we elected to use a 3T DTI-MRI dataset involving 83 ALS patients and 64 healthy subjects [39].Four white-matter tracts were taken into consideration: the orbitofrontal-hypothalamic tract, the insular-hypothalamic tract, the cingulate-hypothalamic tract (Fig. 5) and as reference the corticospinal tract which is known to be substantially altered in ALS patients [39]; the three tracts converging on the hypothalamus were selected because they provided the closest possible match (when accounting for the different anatomy) for the structures investigated in the mouse model and because of their reproducible and unequivocal identification in DTI datasets. We identified a significant decrease in Fractional Anisotropy (FA) of the orbitofrontal-hypothalamic tract in ALS patients (ΔFA = -0.008±0.003; $p<0.05$), with a magnitude approximately one-third of the FA loss in the corticospinal tract (ΔFA = -0.025±0.003; average±SEM, $p<0.001$; Fig. 5). For the cingulate-hypothalamic and insular-hypothalamic tracts, smaller FA losses were detected, which did not reach statistical significance. Thus, disturbances of cortical projections to hypothalamus are not unique characteristics of the mSOD1 murine model of ALS but constitute a previously unrecognized architectural phenotype shared by human ALS patients.

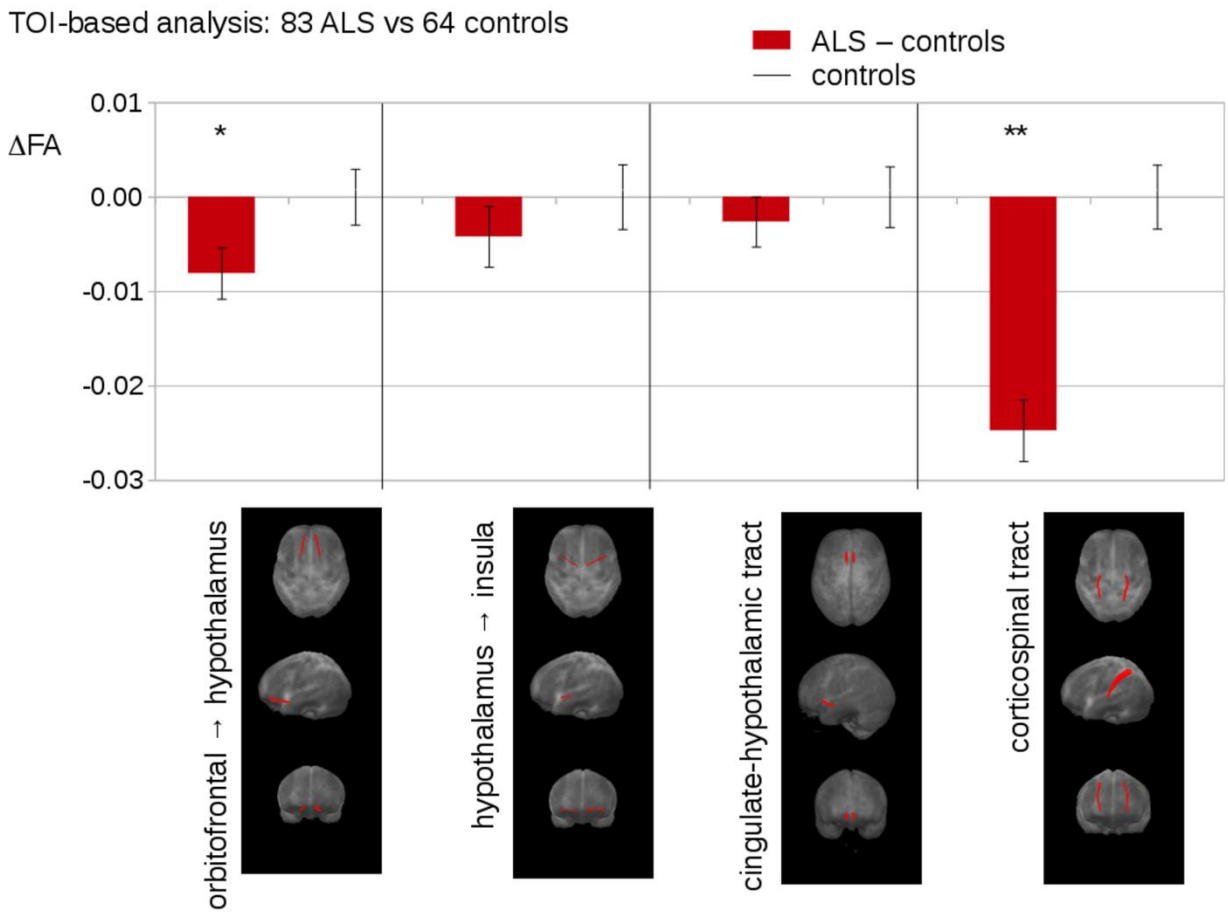

562

563 ***Figure 5***: Tract of Interest (TOI)-based analysis of DTI data from 83 ALS patients vs 64 controls.
564 Upper panel: differences of mean fractional anisotropy (FA) values between ALS patients and
565 controls. Lower panel: projectional views (axial, coronal, sagittal) of tract systems used for TOI
566 analysis. TOI – tract-of-interest; *p < 0.05; **p < 0.001; error bars are the standard error of the
567 mean (SEM).
568

569 **Discussion**

570 Here we provide converging evidence from ALS mouse models and human imaging datasets of
571 the involvement of large-scale projections to LHA in ALS, in particular the disruption of
572 connections from Orbitofrontal Cortex and/or Agranular Insula to LHA. This effect is
573 independent of systematic biases introduced by software or human operators in the
574 registration, does not appear to be an intrinsic developmental defect and it is not detected in an
575 independent ALS model devoid of metabolic phenotypes. The findings in the murine model

display striking similarity to the disruption of the orbitofrontal-hypothalamic tract identified in a large dataset of DTI-MRI of ALS patients.

Hypermetabolism in ALS has been repeatedly reported in human patients [9-13] as well as in some, but not all, ALS murine models [14] and, notably, it appears to develop over time and may predate the clinical onset of disease by several years [3, 46]. Nevertheless, the mechanisms for this clinical manifestation of ALS are unclear.

Direct involvement of the hypothalamus has been hypothesized on the basis of the role of this structure as the main central controller of energy homeostasis, feeding and satiety [47], has been supported by evidence of reduced hypothalamic volume in ALS patients [48] and by the detection of ALS-related TDP-43 pathology in a subset of ALS patients hypothalami [49]. Neurochemical abnormalities, such as reduced MCH expression, have been reported in mutant SOD1 murine models [50]. However, these signs of intrinsic hypothalamic disturbance are not mutually exclusive with the hypothesis that large-scale hypothalami circuits may be dysfunctional, too. Disruption within the larger circuit regulating hypothalamic function, which include insular, motor, orbitofrontal and limbic areas, may contribute to the hypothalamic dysregulation by altering the equilibrium of the different inputs. Indeed, changes in neuronal activity in hypothalamus may produce substantial modifications of the neurochemical identity of local subpopulation, including switch in type of neurotransmitter released [51]. Here we demonstrate that besides any pathology intrinsic to the hypothalamus, the disease pathophysiology involves a substantial quantitative change in the inputs that hypothalamus

receives, particularly from agranular insula and ventrolateral orbitofrontal cortex. This remodeling process coincides with the onset of body weight loss in mSOD1.

Notably, the circuit involving projections from orbitofrontal cortex and agranular insula to lateral hypothalamus is conserved from mice and rats [52, 53] to marmosets [54] and macaques [55] to humans, thus validating mouse as a model organism. Nevertheless, the murine orbitofrontal cortex (including ventral and ventrolateral) and agranular insula are considered homologous of orbitomedial cortex in primates [56], so that the study the orbitofrontal-LHA tract in our DTI tracing study is located more medially than the ORBl/vl+AI complex in the mouse brain.

Remarkably, altered projections from AI/ORBvl in mSOD1 mice correspond to reduced FA in the orbitofrontal-hypothalamic (but not insular-hypothalamic) tract in humans. Although it is noteworthy that abnormalities appear in the same brain structures in animal models and patients with ALS, the closer examination of the findings reveal that in the murine model an actual expansion of projections is detected whereas decreased FA in DTI is usually interpreted as loss of integrity of axons or myelinated tracts [57]. However, it must be stressed that $SOD1^{(G93A)}$ displays a fast progression and becomes symptomatic at a comparatively young age, when the potential for compensatory sprouting after degeneration may be larger than in older human patients (hence, the expansion of the projections). Thus, in human patients the DTI may reveal a change in microstructural integrity resulting from axonal loss but would be unable to detect any increase in the size of axonal arborization.

To the best of our knowledge, there is no demonstration that the orbitofrontal cortex and/or AI can directly regulate metabolic rates. It must be emphasized, though, that lesion studies of these structures have not included a rigorous, long-term testing of body-weight dynamics and inactivation studies have been performed only in short-term settings [58-60]. On the other hand, OFC and AI are involved in processing food characteristics, such as taste, smell and texture [61] and display a differential response to caloric content of food depending on the satiety of the subject (at least in humans: [62, 63]). Thus, it is conceivable that altered connectivity between vlORB/AI and LHA may provide the latter with incorrect inputs regarding the nutritional content of food, contributing to the dysregulation of body metabolic rates. At least in human subjects, reduced volume of grey matter and altered microstructural integrity (measured by apparent diffusion coefficient) in orbitofrontal cortex have been observed in obese patients [64-66], strengthening the link between dysfunction in orbitofrontal cortex and body weight.

Unexpectedly, our retrograde projection mapping strategy has consistently identified projections from primary and secondary motor cortex to LHA, which appear to be affected by the disease process both in mSOD1 and in kiFUS. This connectivity appears to be reciprocal, since LHA projections to motor cortices have also been reported [21]. These connections cannot be easily discounted as artifacts due to the proximity of LHA to the corticospinal tract, since they appear to originate from both ipsi and contralateral hemispheres. It is conceivable that LHA may receive inputs relaying the average motor activity performed or planned and may adjust energy balance accordingly; disruption of connectivity between motor cortex and hypothalamus may

leave the latter "free running", without a proper estimate of current motor activity. Alternatively, it is possible that any pathogenic event in motor cortex (propagating prionoids or abnormal activity patterns) may propagate to hypothalamus and drive its dysfunction and degeneration (as suggested for spinal cord [67]).

Conclusion

Our findings suggest that disruption of large-scale circuits providing input to LHA may contribute to generate the metabolic phenotype observed in ALS; in particular, we have identified the orbitofrontal-hypothalamic tract as a site of convergence of mouse projection data and human tracing data, which may open up an independent approach to evaluate non-motor prognostic features in ALS.

Declarations

Acknowledgements

We thank the colleagues of the German Center for Neurodegenerative Diseases (DZNE)-Ulm for helpful comments.

Authors' contributions

DB contributed to experimental design and performed the stereotactic injections and processed the samples for imaging and performed the image analysis using the WholeBrain registration. SA wrote the image analysis pipeline and performed the manual parcellation study. HPM and JK performed the analysis of the MRI-DTI dataset. AL contributed to the MRI-DTI dataset. FR and JK

663 designed the experiments, analyzed the data and wrote the first version of the manuscript. FR,
664 JK, AL, TB and LD contributed to the final version of the manuscript and to the interpretation of
665 the findings. All authors read and approved the final manuscript.
666
667 *Conflict of interst*
668 The authors declare no financial interest or conflict of interest.
669
670 *Ethics approval and consent to participate*
671 The animal experiments were approved by the Regierungspräsidium Tübingen under the animal
672 license- number 1390 and by the Ulm University Tierforschungszentrum committee.
673 The collection of MRI-DTI data from human subjects has been approved by the Ethical
674 Committee of the University of Ulm (reference #19/12)
675
676 *Availability of data and materials*
677 The datasets used and/or analysed during the current study are available from the
678 corresponding author on reasonable request.
679
680 *Funding*
681 FR is supported by the Thierry Latran Foundation (projects “Trials” and “Hypothals”), by the
682 Radala Foundation, by the Deutsche Forschungsgemeinschaft (DFG, German Research
683 Foundation)- Project-ID 251293561 – Collaborative Research Center (CRC) 1149 and with the
684 individual grant no. 431995586 (RO-5004/8-1) and no. 443642953 (RO5004/9-1), by the Cellular

and Molecular Mechanisms in Aging (CEMMA) Research Training Group and by BMBF (FKZ 01EW1705A, as member of the ERANET-NEURON consortium "MICRONET"). SA and DB are members of the International Graduate School in Molecular Medicine at Ulm University; DB is part of the Graduate School in Cellular and Molecular Mechanisms in Aging at Ulm University.

References:

1) Hardiman O, Al-Chalabi A, Chio A, et al. Amyotrophic lateral sclerosis [published correction appears in Nat Rev Dis Primers. 2017 Oct 20;3:17085]. *Nat Rev Dis Primers*. 2017;3:17071. Published 2017 Oct 5. doi:10.1038/nrdp.2017.71

2) Dupuis L, Pradat PF, Ludolph AC, Loeffler JP. Energy metabolism in amyotrophic lateral sclerosis. *Lancet Neurol*. 2011;10(1):75-82. doi:10.1016/S1474-4422(10)70224-6

3) Peter RS, Rosenbohm A, Dupuis L, et al. Life course body mass index and risk and prognosis of amyotrophic lateral sclerosis: results from the ALS registry Swabia. *Eur J Epidemiol*. 2017;32(10):901-908. doi:10.1007/s10654-017-0318-z

4) Gallo V, Wark PA, Jenab M, et al. Prediagnostic body fat and risk of death from amyotrophic lateral sclerosis: the EPIC cohort. *Neurology*. 2013;80(9):829-838. doi:10.1212/WNL.0b013e3182840689

5) Dupuis L, Corcia P, Fergani A, et al. Dyslipidemia is a protective factor in amyotrophic lateral sclerosis. *Neurology*. 2008;70(13):1004-1009. doi:10.1212/01.wnl.0000285080.70324.27

6) Dorst J, Kühnlein P, Hendrich C, Kassubek J, Sperfeld AD, Ludolph AC. Patients with elevated triglyceride and cholesterol serum levels have a prolonged survival in amyotrophic lateral sclerosis. *J Neurol*. 2011;258(4):613-617. doi:10.1007/s00415-010-5805-z

7) Lindauer E, Dupuis L, Müller HP, Neumann H, Ludolph AC, Kassubek J. Adipose Tissue Distribution Predicts Survival in Amyotrophic Lateral Sclerosis. *PLoS One*. 2013;8(6):e67783. Published 2013 Jun 27. doi:10.1371/journal.pone.0067783

8) Marin B, Desport JC, Kajeu P, et al. Alteration of nutritional status at diagnosis is a prognostic factor for survival of amyotrophic lateral sclerosis patients. *J Neurol Neurosurg Psychiatry*. 2011;82(6):628-634. doi:10.1136/jnnp.2010.211474

9) Steyn FJ, Ioannides ZA, van Eijk RPA, et al. Hypermetabolism in ALS is associated with greater functional decline and shorter survival. *J Neurol Neurosurg Psychiatry*. 2018;89(10):1016-1023. doi:10.1136/jnnp-2017-317887

10) Jésus P, Fayemendy P, Nicol M, et al. Hypermetabolism is a deleterious prognostic factor in patients with amyotrophic lateral sclerosis. *Eur J Neurol*. 2018;25(1):97-104. doi:10.1111/ene.13468

11) Ahmed RM, Irish M, Piguet O, et al. Amyotrophic lateral sclerosis and frontotemporal dementia: distinct and overlapping changes in eating behaviour and metabolism [published correction appears in Lancet Neurol. 2016 Apr;15(4):352]. *Lancet Neurol*. 2016;15(3):332-342. doi:10.1016/S1474-4422(15)00380-4

12) Desport JC, Torny F, Lacoste M, Preux PM, Couratier P. Hypermetabolism in ALS: correlations with clinical and paraclinical parameters. *Neurodegener Dis*. 2005;2(3-4):202-207. doi:10.1159/000089626

13) Bouteloup C, Desport JC, Clavelou P, et al. Hypermetabolism in ALS patients: an early and persistent phenomenon. *J Neurol*. 2009;256(8):1236-1242. doi:10.1007/s00415-009-5100-z

14) Dupuis L, Oudart H, René F, Gonzalez de Aguilar JL, Loeffler JP. Evidence for defective energy homeostasis in amyotrophic lateral sclerosis: benefit of a high-energy diet in a transgenic mouse model. *Proc Natl Acad Sci U S A*. 2004;101(30):11159-11164. doi:10.1073/pnas.0402026101

15) Ludolph AC, Dorst J, Dreyhaupt J, et al. Effect of High-Caloric Nutrition on Survival in Amyotrophic Lateral Sclerosis. *Ann Neurol*. 2020;87(2):206-216. doi:10.1002/ana.25661

16) González JA, Iordanidou P, Strom M, Adamantidis A, Burdakov D. Awake dynamics and brain-wide direct inputs of hypothalamic MCH and orexin networks. *Nat Commun*. 2016;7:11395. Published 2016 Apr 22. doi:10.1038/ncomms11395

17) Barbier M, Chometton S, Pautrat A, et al. A basal ganglia-like cortical-amygdalar-hypothalamic network mediates feeding behavior. *Proc Natl Acad Sci U S A*. 2020;117(27):15967-15976. doi:10.1073/pnas.2004914117

18) Barbier M, González JA, Houdayer C, Burdakov D, Risold PY, Croizier S. Projections from the dorsomedial division of the bed nucleus of the stria terminalis to hypothalamic nuclei in the mouse [published online ahead of print, 2020 Jul 17]. *J Comp Neurol*. 2020;10.1002/cne.24988. doi:10.1002/cne.24988

19) Murata K, Kinoshita T, Fukazawa Y, et al. GABAergic neurons in the olfactory cortex projecting to the lateral hypothalamus in mice. *Sci Rep*. 2019;9(1):7132. Published 2019 May 9. doi:10.1038/s41598-019-43580-1

20) Berthoud HR. Multiple neural systems controlling food intake and body weight. *Neurosci Biobehav Rev*. 2002;26(4):393-428. doi:10.1016/s0149-7634(02)00014-3

21) Commisso B, Ding L, Varadi K, et al. Stage-dependent remodeling of projections to motor cortex in ALS mouse model revealed by a new variant retrograde-AAV9. *Elife*. 2018;7:e36892. Published 2018 Aug 23. doi:10.7554/eLife.36892

22) Agosta F, Canu E, Valsasina P, et al. Divergent brain network connectivity in amyotrophic lateral sclerosis. *Neurobiol Aging*. 2013;34(2):419-427. doi:10.1016/j.neurobiolaging.2012.04.015

23) Schulthess I, Gorges M, Müller HP, et al. Functional connectivity changes resemble patterns of pTDP-43 pathology in amyotrophic lateral sclerosis. *Sci Rep*. 2016;6:38391. Published 2016 Dec 8. doi:10.1038/srep38391

24) Heimrath J, Gorges M, Kassubek J, et al. Additional resources and the default mode network: Evidence of increased connectivity and decreased white matter integrity in amyotrophic lateral sclerosis. *Amyotroph Lateral Scler Frontotemporal Degener*. 2014;15(7-8):537-545. doi:10.3109/21678421.2014.911914

25) Dukic S, McMackin R, Buxo T, et al. Patterned functional network disruption in amyotrophic lateral sclerosis. *Hum Brain Mapp*. 2019;40(16):4827-4842. doi:10.1002/hbm.24740

26) Braak H, Brettschneider J, Ludolph AC, Lee VM, Trojanowski JQ, Del Tredici K. Amyotrophic lateral sclerosis--a model of corticofugal axonal spread. *Nat Rev Neurol*. 2013;9(12):708-714. doi:10.1038/nrneurol.2013.221

27) Brettschneider J, Del Tredici K, Toledo JB, et al. Stages of pTDP-43 pathology in amyotrophic lateral sclerosis. *Ann Neurol*. 2013;74(1):20-38. doi:10.1002/ana.23937

28) Scekic-Zahirovic J, Sendscheid O, El Oussini H, et al. Toxic gain of function from mutant FUS protein is crucial to trigger cell autonomous motor neuron loss. *EMBO J*. 2016;35(10):1077-1097. doi:10.15252/embj.201592559

29) Ouali Alami N, Schurr C, Olde Heuvel F, et al. NF-κB activation in astrocytes drives a stage-specific beneficial neuroimmunological response in ALS. *EMBO J*. 2018;37(16):e98697. doi:10.15252/embj.201798697

30) Tervo DG, Hwang BY, Viswanathan S, et al. A Designer AAV Variant Permits Efficient Retrograde Access to Projection Neurons. *Neuron*. 2016;92(2):372-382. doi:10.1016/j.neuron.2016.09.021

31) Madisen L, Garner AR, Shimaoka D, et al. Transgenic mice for intersectional targeting of neural sensors and effectors with high specificity and performance. *Neuron*. 2015;85(5):942-958. doi:10.1016/j.neuron.2015.02.022

32) Paxinos G, Franklin KBJ. The mouse brain in stereotaxic coordinates, second edition. (*ACADEMIC PRESS*, 2001), ISBN: 0-12-547636-1

33) Schindelin J, Arganda-Carreras I, Frise E, et al. Fiji: an open-source platform for biological-image analysis. *Nat Methods*. 2012;9(7):676-682. Published 2012 Jun 28. doi:10.1038/nmeth.2019

34) Fürth D, Vaissière T, Tzortzi O, et al. An interactive framework for whole-brain maps at cellular resolution [published correction appears in Nat Neurosci. 2017 Dec 18;:]. *Nat Neurosci*. 2018;21(1):139-149. doi:10.1038/s41593-017-0027-7

35) Lein ES, Hawrylycz MJ, Ao N, et al. Genome-wide atlas of gene expression in the adult mouse brain. *Nature*. 2007;445(7124):168-176. doi:10.1038/nature05453

36) Berg S, Kutra D, Kroeger T, et al. ilastik: interactive machine learning for (bio)image analysis. *Nat Methods*. 2019;16(12):1226-1232. doi:10.1038/s41592-019-0582-9

37) Fiaschi L, Koethe U, Nair R, Hamprecht FA. Learning to count with regression forest and structured labels. *Proceedings of the 21st International Conference on Pattern Recognition (ICPR2012)*, Tsukuba, 2012;2685-2688.

38) Sahoo P, Wilkins C, Yeager J. Threshold selection using Renyi's entropy. Pattern Recognition. 1997;30(1):71-84. doi:10.1016/S0031-3203(96)00065-9

39) Kassubek J, Müller HP, Del Tredici K, et al. Imaging the pathoanatomy of amyotrophic lateral sclerosis in vivo: targeting a propagation-based biological marker. *J Neurol Neurosurg Psychiatry*. 2018;89(4):374-381. doi:10.1136/jnnp-2017-316365

40) Müller HP, Unrath A, Ludolph AC, Kassubek J. Preservation of diffusion tensor properties during spatial normalization by use of tensor imaging and fibre tracking on a normal brain database. *Phys Med Biol*. 2007;52(6):N99-N109. doi:10.1088/0031-9155/52/6/N01

41) Müller HP, Del Tredici K, Lulé D, et al. In vivo histopathological staging in C9orf72-associated ALS: A tract of interest DTI study. *Neuroimage Clin*. 2020;27:102298. doi:10.1016/j.nicl.2020.102298

42) Müller HP, Unrath A, Sperfeld AD, Ludolph AC, Riecker A, Kassubek J. Diffusion tensor imaging and tractwise fractional anisotropy statistics: quantitative analysis in white matter pathology. *Biomed Eng Online*. 2007;6:42. Published 2007 Nov 9. doi:10.1186/1475-925X-6-42

43) Petrik MS, Wilson JM, Grant SC, et al. Magnetic resonance microscopy and immunohistochemistry of the CNS of the mutant SOD murine model of ALS reveals widespread neural deficits. *Neuromolecular Med*. 2007;9(3):216-229. doi:10.1007/s12017-007-8002-1

44) Pickles S, Destroismaisons L, Peyrard SL, et al. Mitochondrial damage revealed by immunoselection for ALS-linked misfolded SOD1. *Hum Mol Genet*. 2013;22(19):3947-3959. doi:10.1093/hmg/ddt249

45) Scekic-Zahirovic J, Oussini HE, Mersmann S, et al. Motor neuron intrinsic and extrinsic mechanisms contribute to the pathogenesis of FUS-associated amyotrophic lateral sclerosis. *Acta Neuropathol*. 2017;133(6):887-906. doi:10.1007/s00401-017-1687-9

46) Mariosa D, Beard JD, Umbach DM, et al. Body Mass Index and Amyotrophic Lateral Sclerosis: A Study of US Military Veterans. *Am J Epidemiol*. 2017;185(5):362-371. doi:10.1093/aje/kww140

47) Vercruysse P, Vieau D, Blum D, Petersén Å, Dupuis L. Hypothalamic Alterations in Neurodegenerative Diseases and Their Relation to Abnormal Energy Metabolism. *Front Mol Neurosci*. 2018;11:2. Published 2018 Jan 19. doi:10.3389/fnmol.2018.00002

48) Gorges M, Vercruysse P, Müller HP, et al. Hypothalamic atrophy is related to body mass index and age at onset in amyotrophic lateral sclerosis. *J Neurol Neurosurg Psychiatry*. 2017;88(12):1033-1041. doi:10.1136/jnnp-2017-315795

49) Cykowski MD, Takei H, Schulz PE, Appel SH, Powell SZ. TDP-43 pathology in the basal forebrain and hypothalamus of patients with amyotrophic lateral sclerosis. *Acta Neuropathol Commun*. 2014;2:171. Published 2014 Dec 24. doi:10.1186/s40478-014-0171-1

50) Vercruysse P, Sinniger J, El Oussini H, et al. Alterations in the hypothalamic melanocortin pathway in amyotrophic lateral sclerosis. *Brain*. 2016;139(Pt 4):1106-1122. doi:10.1093/brain/aww004

51) Meng D, Li HQ, Deisseroth K, Leutgeb S, Spitzer NC. Neuronal activity regulates neurotransmitter switching in the adult brain following light-induced stress. Proc Natl Acad Sci U S A. 2018 May 15;115(20):5064-5071.

52) Floyd NS, Price JL, Ferry AT, Keay KA, Bandler R. Orbitomedial prefrontal cortical projections to hypothalamus in the rat. *J Comp Neurol*. 2001;432(3):307-328. doi:10.1002/cne.1105

53) Hoover WB, Vertes RP. Projections of the medial orbital and ventral orbital cortex in the rat. *J Comp Neurol*. 2011;519(18):3766-3801. doi:10.1002/cne.22733

54) Roberts AC, Tomic DL, Parkinson CH, et al. Forebrain connectivity of the prefrontal cortex in the marmoset monkey (Callithrix jacchus): an anterograde and retrograde tract-tracing study. *J Comp Neurol*. 2007;502(1):86-112. doi:10.1002/cne.21300

55) Ongür D, An X, Price JL. Prefrontal cortical projections to the hypothalamus in macaque monkeys. *J Comp Neurol*. 1998;401(4):480-505.

56) Price JL. Definition of the orbital cortex in relation to specific connections with limbic and visceral structures and other cortical regions. *Ann N Y Acad Sci*. 2007;1121:54-71. doi:10.1196/annals.1401.008

57) Alexander AL, Lee JE, Lazar M, Field AS. Diffusion tensor imaging of the brain. *Neurotherapeutics*. 2007;4(3):316-329. doi:10.1016/j.nurt.2007.05.011

58) Kobayashi M. Macroscopic connection of rat insular cortex: anatomical bases underlying its physiological functions. *Int Rev Neurobiol*. 2011;97:285-303. doi:10.1016/B978-0-12-385198-7.00011-4

59) Izquierdo A. Functional Heterogeneity within Rat Orbitofrontal Cortex in Reward Learning and Decision Making. *J Neurosci*. 2017;37(44):10529-10540. doi:10.1523/JNEUROSCI.1678-17.2017

60) Rolls ET. The functions of the orbitofrontal cortex. *Brain Cogn*. 2004;55(1):11-29. doi:10.1016/S0278-2626(03)00277-X

61) Seabrook LT, Borgland SL. The orbitofrontal cortex, food intake and obesity. *J Psychiatry Neurosci*. 2020;45(5):304-312. doi:10.1503/jpn.190163

62) Schur EA, Kleinhans NM, Goldberg J, Buchwald D, Schwartz MW, Maravilla K. Activation in brain energy regulation and reward centers by food cues varies with choice of visual stimulus. *Int J Obes (Lond)*. 2009;33(6):653-661. doi:10.1038/ijo.2009.56

63) Suzuki S, Cross L, O'Doherty JP. Elucidating the underlying components of food valuation in the human orbitofrontal cortex. *Nat Neurosci*. 2017;20(12):1780-1786. doi:10.1038/s41593-017-0008-x

64) Raji CA, Ho AJ, Parikshak NN, et al. Brain structure and obesity. *Hum Brain Mapp*. 2010;31(3):353-364. doi:10.1002/hbm.20870

65) Walther K, Birdsill AC, Glisky EL, Ryan L. Structural brain differences and cognitive functioning related to body mass index in older females. *Hum Brain Mapp*. 2010;31(7):1052-1064. doi:10.1002/hbm.20916

66) Alkan A, Sahin I, Keskin L, et al. Diffusion-weighted imaging features of brain in obesity. *Magn Reson Imaging*. 2008;26(4):446-450. doi:10.1016/j.mri.2007.10.004

67) Burg T, Bichara C, Scekic-Zahirovic J, et al. Absence of Subcerebral Projection Neurons Is Beneficial in a Mouse Model of Amyotrophic Lateral Sclerosis [published online ahead of print, 2020 Jun 26]. *Ann Neurol*. 2020;10.1002/ana.25833. doi:10.1002/ana.25833

954 **Supplementary:**

955 **Supplementary *Table 1***: Anatomical landmarks used for mapping the brain section from
956 anterior to posterior. The following structures provided distinctive optical characteristics for
957 mapping: AOB = Accessory olfactory bulb; DP = Dorsal peduncular area; fa = corpus callosum,
958 anterior forceps; ccg = genu of corpus callosum; aco = anterior commissure, olfactory limb; act =
959 anterior commissure, temporal limb; SCH = Suprachiasmatic nucleus; NLOT = Nucleus of the
960 lateral olfactory tract; ME = Median eminence; opt = optic tract; int = internal capsule; DG =
961 Dentate gyrus; CA3so = Field CA3, stratum oriens; MM = Medial mammillary nucleus.
962

Coordinate from bregma	Anatomical landmark	Section in Allen´s brain atlas
2,6	first section without AOB	27
2,2	section before beginning of DP	32
2,1	first section with DP	33
1,6	shape of fa	38
1,5	shape of fa	39
1,4	shape of fa	40
1,2	shape of fa	42
1,1	shape of fa	43
1	shape of ccg	44
0,2	shape of aco	52
0,1	shape of aco	53
0	shape of aco and act	54
-0,3	first section with SCH last section without NLOT	57
-1	shape of opt last section with NLOT	64
-1,4	first section with ME shape of otp and int	69
-2,2	first section without ME first section with ventral DG	76
-2,5	Expansion of CA3so	79
-3,1	last section with MM	85

963
964

965 ***Supplementary Table 2***: List of structures of the brain projecting to LHA. For each structure, the
966 absolute number of neurons projecting to LHA is reported as mean ± SD and independently for
967 ipsi- and contralateral hemispheres.
968

	Ipsilateral raw data	Contralateral raw data	Ipsilateral normalized	Contralateral normalized
A13	85.6, ±45.9	10.4, ±6.6	58.5, ±28.2	7.1, ±3.8
AAA	297.6, ±230.0	18.8, ±7.2	225.3, ±128.1	16.3, ±7.4
ACA	2686.2, ±1373.5	897.0, ±468.9	1826.0, ±538.9	599.4, ±232.6
ACB	565.4, ±375.1	9.4, ±10.1	411.8, ±173.1	7.9, ±6.9
ADP	64.4, ±27.3	16.6, ±8.6	48.3, ±10.8	12.5, ±4.1
AHN	1174.0, ±1241.1	111.4, ±91.1	909.7, ±1146.0	84.7, ±77.7
AI	1437.8, ±1365.3	197.0, ±177.6	935.9, ±622.2	117.2, ±82.2
AON	92.2, ±90.1	6.2, ±4.4	64.6, ±41.4	4.1, ±1.6
APN	54.2, ±43.3	5.4, ±1.7	35.4, ±19.1	5.7, ±4.8
AUD	228.6, ±246.6	62.2, ±48.6	138.4, ±129.3	38.0, ±27.4
AVP	207.8, ±99.8	71.6, ±36.0	143.2, ±41.5	49.3, ±22.1
AVPV	242.0, ±43.6	71.2, ±31.5	216.0, ±99.8	70.5, ±57.7
BLA	1263.0, ±670.4	79.6, ±56.3	920.2, ±278.5	52.6, ±28.0
BMA	1405.0, ±744.5	110.4, ±67.5	1009.6, ±381.6	77.4, ±37.9
BST	2108.8, ±774.0	275.6, ±165.1	1613.9, ±236.4	188.0, ±82.2
CEA	440.4, ±315.9	14.4, ±6.8	292.6, ±129.9	12.6, ±7.0
CLA	20.0, ±11.5	4.4, ±2.2	14.8, ±4.9	3.8, ±2.1
CM	132.8, ±65.5	49.2, ±18.7	97.1, ±40.2	37.5, ±7.1
COA	730.4, ±377.3	39.2, ±31.1	539.2, ±179.2	25.4, ±17
CP	814.4, ±499.4	34.8, ±21.2	581.7, ±185.8	23.0, ±7.0
DMH	1510.0, ±729.1	233.8, ±115.7	1039.7, ±290.7	160.3, ±50
DP	618.4, ±249.1	192.2, ±128.9	535.8, ±289.4	131.5, ±54.3
ECT	255.8, ±139.4	79.0, ±50.1	172.5, ±48.9	50.5, ±26.3
ENTl	144.8, ±96.2	28.6, ±18.1	98.2, ±46.0	18.1, ±10.3
EP	252.0, ±241.5	9.4, ±8.1	175.9, ±109.7	5.8, ±4.8
FS	59.8, ±45.7	1.0, ±0.9	48.2, ±31.9	0.7, ±0.7
GP	133.8, ±83.9	9.8, ±10.7	90.2, ±27.0	6.0, ±5.3
GU	503.2, ±399.3	77.0, ±63.8	343.9, ±186.6	49.7, ±28.3
IA	127.4, ±90.9	8.0, ±5.8	92.8, ±70.4	6.5, ±5.0
ILA	2627.2, ±896.1	1192.2, ±548.6	2089.0, ±476.3	834.9, ±188.3
IMD	145.8, ±74.4	55.8, ±29.8	103.6, ±34.6	37.5, ±11.9
LH	188.4, ±99.4	32.6, ±17.2	127.9, ±41.1	21.8, ±9.0
LHA	Injection	845.8, ±509.0	Injection	573.8, ±167.2
LPO	1251.6, ±447.7	173.2, ±113.4	1000.5, ±271.0	120.5, ±51.3
LS	1453.4, ±583.2	179.6, ±78.9	1169.3, ±436.5	127.3, ±23.3
MA	139.6, ±177.3	5.8, ±4.1	97.8, ±90.1	6.0, ±6.1

MEA	712.8, ±691.0	72.4, ±103.5	499.2, ±437.3	46.6, ±66.8
MEPO	252.8, ±96.0	204.6, ±71.7	207.2, ±71.9	169.9, ±57.2
MM	126.0, ±105.5	55.2, ±49.2	86.8, ±54.7	36.4, ±29.1
MOp	1006.4, ±1321.7	71.6, ±74.0	576.5, ±705.8	40.4, ±38.2
MOs	2292.6, ±2310.5	273.6, ±224.4	1391.5, ±1146.2	168.8, ±103.4
MPN	701.2, ±246.6	177.2, ±104.2	551.6, ±124.7	121.4, ±56.4
MPO	1752.4, ±543.1	436.4, ±213.4	1384.5, ±259.7	306.7, ±83.4
MS	323.0, ±157.8	58.4, ±29.3	240.5, ±56.7	47.0, ±16.7
NDB	288.2, ±281.3	34.4, ±24.5	202.7, ±126.0	24.7, ±20.6
NLOT	74.0, ±40.3	8.0, ±5.4	55.9, ±20.7	5.5, ±3.1
OLF	125.4, ±76.6	19.0, ±11.4	97.4, ±39.3	13.5, ±4.9
ORBl	306.6, ±425.5	41.8, ±68.5	168.7, ±213.7	22.7, ±34.6
ORBm	515.4, ±261.3	142.6, ±120.6	421.2, ±183.3	104.2, ±53.7
ORBvl	184.8, ±193.9	31.4, ±42.7	110.2, ±90.7	18.6, ±20.7
OT	58.4, ±74.6	1.8, ±1.7	37.9, ±35.2	1.5, ±1.0
OV	28.2, ±9.0	17.2, ±4.2	24.9, ±12.4	16.2, ±9.8
PA	398.4, ±541.0	156.2, ±271.9	252.9, ±347.2	99.8, ±175.5
PAA	31.2, ±11.4	2.6, ±0.8	25.3, ±7.4	2.5, ±1.5
PD	17.8, ±7.0	3.6, ±3.8	14.7, ±5.9	2.6, ±2.3
PERI	235.0, ±141.4	60.8, ±34.0	156.4, ±61.6	39.9, ±15.5
PH	1304.0, ±428.6	662.0, ±209.6	1043.6, ±248.9	528.6, ±123.8
PIR	667.0, ±677.1	27.0, ±12.9	444.4, ±302.3	20.2, ±6.7
PL	1576.0, ±554.1	653.6, ±330.0	1239.8, ±254.5	466.9, ±93.6
PS	33.2, ±20.0	2.8, ±2.5	22.2, ±6.3	1.8, ±1.5
PST	37.0, ±26.9	4.0, ±4.6	41.3, ±47.5	2.9, ±2.5
PSTN	160.2, ±59.7	16.6, ±12.9	168.5, ±158.2	11.4, ±5.6
PTL	199.4, ±198.2	17.0, ±11.1	121.9, ±104.4	11.2, ±5.0
PV	239.8, ±164.1	46.2, ±27.2	171.9, ±111.7	34.1, ±14.2
PVH	449.2, ±210.4	72.4, ±46.7	339.2, ±164.4	50.9, ±33.3
PVT	960.4, ±475.5	332.4, ±231.1	686.5, ±334.9	242.4, ±193.1
RE	461.0, ±379.7	176.4, ±122.5	356.0, ±347.2	134.9, ±109.3
RSP	331.8, ±297.9	47.6, ±32.1	198.7, ±152.4	30.7, ±15.4
SF	57.8, ±32.7	13.6, ±6.0	41.9, ±21.1	9.7, ±3.6
SI	1278.0, ±723.9	71.8, ±65.0	982.8, ±364.2	46.3, ±28.1
SS	700.6, ±860.7	57.4, ±49.5	407.5, ±454	40.5, ±25.0
STN	124.4, ±78.1	20.0, ±11.8	116.4, ±96.7	13.2, ±5.1
SUM	475.2, ±235.5	211.4, ±145.1	370.8, ±110.8	144.5, ±54.0
TEa	205.6, ±122.0	78.6, ±58.0	136.7, ±45.9	49.3, ±29.6
TRS	27.8, ±18.0	20.4, ±19.1	24.1, ±16.7	14.6, ±11.3
TT	929.4, ±512.0	214.6, ±194.3	802.0, ±531.2	131.0, ±95.0
TU	531.4, ±445.1	60.8, ±36.4	353.3, ±263.6	41.7, ±18.4
VIS	68.4, ±49.9	5.0, ±4.1	42.7, ±26.3	3.6, ±3.7

VISC	138.6, ±109.1	22.0, ±21.0	86.0, ±49.0	14.3, ±9.3
VLPO	57.4, ±30.1	17.8, ±15.3	40.3, ±11.4	11.3, ±9.3
VM	821.2, ±745.3	84.8, ±34.6	523.4, ±351.8	63.8, ±20.3
VMH	1462.6, ±799.9	187.4, ±149.2	1004.7, ±629.3	137.7, ±133.4
VP	163.2, ±158.4	28.0, ±12.4	110.7, ±75.8	21.4, ±5.6
ZI	1829.0, ±912.2	263.0, ±107.7	1374.4, ±334.2	194.9, ±34.7

Supplementary Figure 1-9 are provided in a separate PDF

Supplementary Fig. 1: Altered cortico-hypothalamic projection pattern in mSOD1 mice at P95, absolute counts ipsilateral. A: Sum of neurons projecting from selected 28 areas. Significantly increased projections from ipsilateral hemisphere in mSOD mice to LHA (p=0.02; n=3). B: Quantification of the absolute number of neurons projecting to LHA from 28 brain structures in WT and mSOD1. A significant increase in projections from ACA (p<0.0001), ILA (p=0.009), ORBl/vl+AI (p<0.0001), Tenia Tecta (TT; p=0.0365), secondary Motor Cortex (MOs, p<0.0001) and Piriform cortex (PIR; p=0.0005). C: Representative *WholeBrain* ipsilateral side view reconstructions of neurons projecting to LHA in WT and mSOD1 mice. Expansion of projections from MOs are visible (arrows). D: Representative *WholeBrain* cortical top view reconstructions of neurons projecting to LHA in WT and mSOD1 mice. Expansion of projections from MOs are visible (arrows). Bars show mean ± SD. *p < 0.05, **p < 0.01, ***p < 0.001, ****p< 0.0001.

Supplementary Fig. 2: Altered cortico-hypothalamic projection pattern in mSOD1 mice at P95, contralateral hemisphere. A: Sum of neurons projecting from selected 28 areas. No difference is detected in the summarized number of neurons projecting to LHA in WT and mSOD1 from the contralateral hemisphere (n=3). B: Quantification of the absolute number of neurons projecting to LHA from 28 brain structures in WT and mSOD1. A significant increase in projections from ACA (p=0.0008), PL+ORBm and ILA (both p<0.0001) is detected. C: No difference is detected in the quantification of the normalized number of neurons projecting to LHA from 28 brain structures in WT and mSOD1. Bars show mean ± SD. *p < 0.05, **p < 0.01, ***p < 0.001, ****p< 0.0001.

Supplementary Fig. 3: Primary motor cortex and somatosensory cortex atrophy in P95 mSOD mice. Volumetric comparison of 28 areas in WT and mSOD. Significant atrophy was detected in MOp and SS. Bars show mean ± SD. *p < 0.05, **p < 0.01, ***p < 0.001, ****p< 0.0001.

Supplementary Fig. 4: Altered cortico-hypothalamic projection pattern in manual registered mSOD1 mice at P95, ipsilateral. A: Left: representative injection sites in LHA for WT and mSOD1 mice. White outlines represent LHA boundaries. Middle and right: Representative frontal brain sections of WT and mSOD1 mice depicting projections from ORBl/vl+AI (significantly increased, arrow), PL+ORBm, ILA, ACA, MOs and MOp to LHA. B: Sum of neurons projecting from selected 28 areas. No difference is detected in the summarized number of neurons projecting to LHA in WT and mSOD1 from the ipsilateral hemisphere (n=3). C: Quantification of the absolute number of neurons projecting to LHA from 28 brain structures in WT and mSOD1. A significant increase

in projections from ORBl/vl+AI (p=0.035) is detected. D: Quantification of the normalized number of neurons projecting to LHA from 28 brain structures in WT and mSOD1. A significant increase in projections from ILA (p=0.001) , ORBl/vl+AI (p<0.0001) and PIR (p<0.0001) is detected. Bars show mean ± SD. Scalebars 1 mm. *p < 0.05, **p < 0.01, ***p < 0.001, ****p< 0.0001.

Supplementary Fig. 5: Altered projection pattern in manual registered mSOD1 mice at P95, contralateral. A: Sum of neurons projecting from selected 28 areas. No difference is detected in the summarized number of neurons projecting to LHA in WT and mSOD1 from the contralateral hemisphere (n=3). B: No difference is detected in the quantification of the absolute number of neurons projecting to LHA from 28 brain structures in WT and mSOD1. C: Quantification of the normalized number of neurons projecting to LHA from 28 brain structures in WT and mSOD1. A significant increase in projections from PL+ORBm (p<0.0001) is detected. Bars show mean ± SD. *p < 0.05, **p < 0.01, ***p < 0.001, ****p< 0.0001.

Supplementary Fig. 6: Unaltered cortico-hypothalamic projection pattern in mSOD1 mice at P25, ipsilateral. A: Left: representative injection sites in LHA for WT and mSOD1 mice. White outlines represent LHA boundaries. Middle and right: Representative frontal brain sections of WT and mSOD1 mice depicting a similar pattern of neurons. B: Sum of neurons projecting from selected 28 areas. No difference is detected in the summarized number of neurons projecting to LHA in WT and mSOD1 from the ipsilateral hemisphere (n=3). C: No difference is detected in the quantification of the absolute number of neurons projecting to LHA from 28 brain structures in WT and mSOD1. D: No difference is detected in the quantification of the normalized number of neurons projecting to LHA from 28 brain structures in WT and mSOD1. Bars show mean ± SD. Scalebars 1 mm.

Supplementary Fig. 7: Unaltered cortico-hypothalamic projection pattern in mSOD1 mice at P25, contralateral hemisphere. A: Sum of neurons projecting from selected 28 areas. No difference is detected in the summarized number of neurons projecting to LHA in WT and mSOD1 from the contralateral hemisphere (n=3). B: Quantification of the absolute number of neurons projecting to LHA from 28 brain structures in WT and mSOD1. A significant increase in projections from ACA (p=0.0078) is detected. C: Quantification of the normalized number of neurons projecting to LHA from 28 brain structures in WT and mSOD1. No difference is detected in the quantification of the number of neurons projecting to LHA from 28 brain structures in WT and mSOD1. D: Representative *WholeBrain* volume reconstructions of neurons projecting to LHA in WT and mSOD1 mice show a similar pattern of projections in MOs (blue), ORBl/vl+AI (yellow) and PL+AI (green). Bars show mean ± SD. *p < 0.05, **p < 0.01, ***p < 0.001, ****p< 0.0001.

Supplementary Fig. 8: Altered cortico-hypothalamic projection pattern in kiFUS mice at P270, absolute counts ipsilateral. A: Sum of neurons projecting from selected 28 areas. No difference is detected in the summarized number of neurons projecting to LHA in WT and kiFUS from the ipsilateral hemisphere (n=4). B: Quantification of the absolute number of neurons projecting to LHA from 28 brain structures in WT and mSOD1. A significant increase in projections from ACA

(p=0.0385) and MOs (p<0.0001) is detected. C: Representative *WholeBrain* ipsilateral side view reconstructions of neurons projecting to LHA in WT and mSOD1 mice. Decrease of projections from MOs are visible (arrows). D: Representative *WholeBrain* cortical top view reconstructions of neurons projecting to LHA in WT and mSOD1 mice. Decrease of projections from MOs are visible (arrows). Bars show mean ± SD. *$p < 0.05$, **$p < 0.01$, ***$p < 0.001$, ****$p< 0.0001$.

Supplementary Fig. 9: Altered cortico-hypothalamic projection pattern in kiFUS mice at P270, contralateral hemisphere. A: Sum of neurons projecting from selected 28 areas. No difference is detected in the summarized number of neurons projecting to LHA in WT and kiFUS from the contralateral hemisphere (n=3). B: Quantification of the absolute number of neurons projecting to LHA from 28 brain structures in WT and mSOD1. A significant increase in projections from ACA (p=0.0121) and ILA (p=0.0474) is detected. C: Quantification of the normalized number of neurons projecting to LHA from 28 brain structures in WT and kiFUS. A significant decrease in projections from ACA (p=0.0137) is detected. Bars show mean ± SD. *$p < 0.05$, **$p < 0.01$, ***$p < 0.001$, ****$p< 0.0001$.

Abbreviations

ABA = Allen brain atlas, version 2011
ACA = Anterior cingulate area
aco = anterior commissure olfactory limb
act = anterior commissure temporal limb
AI = Agranular insular area
ALS = Amyotrophic lateral sclerosis
ALS-FRS-R = ALS functional rating scale revised
AOB = Accessory olfactory bulb
AP = Anteroposterior
AUD = Auditory areas
BLA = Basolateral amygdalar nucleus
BMA = Basolateral amygdalar nucleus
BSA = Bovine serum albumin
CA3so = Field CA3 stratum oriens
ccg = genu of corpus callosum
CLA = Claustrum
COA = Cortical amygdalar area
DG = Dentate gyrus
DP = Dorsal peduncular area
DPBS = Dulbecco's phosphate buffered saline
DTI = Diffusion-tensor-imaging
DV = Dorsoventral
EP = Endopiriform nucleus
fa = corpus callosum anterior forceps
FA = Fractional anisotropy

FUS = B6.FUS$^{\Delta NLS/+}$
HSB = Hue-saturation-brightness color model
GU = Gustatory areas
HY = Hypothalamus
ILA = Infralimbic area
int = internal capsule
kiFUS = FUS^{-}/ZsGreen$^{+/-}$
LA = Lateral amygdalar nucleus
LHA = Lateral hypothalamic area
ME = Median eminence
ML = Mediolateral
MM = Medial mammillary nucleus
MOp = Primary motor area
MOs = Secondary motor area
MRI = Magnetic resonance imaging
mSOD1 = mSOD^{+}/ZsGreen$^{+/-}$
mSOD = B6SJL73 Tg(SOD1*G93A)1Gur/J (high-copy)
NLOT = Nucleus of the lateral olfactory tract
OCT = Optimal cutting temperature compound
opt = optic tract
ORBl/vl = Orbital area, lateral/ventrolateral part
ORBl/vl+ AI = Group of Orbital area, lateral/ventrolateral part and Agranular insular area
ORBm = Orbital area, medial part
OT = Olfactory tubercle
P110 = Post-natal day 110
PA = Posterior amygdalar nucleus
PAA = Piriform-amygdalar area
PBS = Phosphate buffered saline
PFA = Paraformaldehyde
PIR = Piriform area
PL = Prelimbic area
PL+ ORBm = Group of Prelimbic area and Orbital area, medial part
PTL = Posterior parietal association areas
rAAV = recombinant adeno-associated virus
rAAV2-retro = retrograde recombinant adeno-associated virus 2
RAM = Random-access memory
RGB = Red-green-blue color model
Rhinal CTX = Group of Perirhinal area, Ectorhinal area and Entorhinal area, lateral part
ROI = Region of Interest
RSP = Retrosplenial area
rt = room temperature
SCH = Suprachiasmatic nucleus
SS = Somatosensory areas
Tea = Temporal association areas

TFAS = Tractwise fractional anisotropy statistics
tiff = Tagged image file format
TOI = Tract-of-interest
TT = Taenia tecta
VIS = Visual areas
VISC = Visceral area